Nano Energy 67 (2020) 104172

Contents lists available at ScienceDirect

Nano Energy

journal homepage: http://www.elsevier.com/locate/nanoen

Full paper

Uniform lithium electrodeposition for stable lithium-metal batteries

Xin He [a,d], Yang Yang [b], Marian Stan Cristian [c], Jun Wang [c], Xu Hou [a], Bo Yan [a], Jinke Li [a], Tong Zhang [a], Elie Paillard [a,**], Michal Swietoslawski [d], Robert Kostecki [d,***], Martin Winter [a,c], Jie Li [a,*]

[a] Helmholtz Institute Münster – Forschungszentrum Jülich GmbH (IEK 12), Corrensstrasse 46, 48149 Münster, D-48149, Münster, Germany
[b] European Synchrotron Radiation Facility, 71 Avenue des Martyrs, 38000, Grenoble, France
[c] MEET Battery Research Center, Institute of Physical Chemistry, University of Münster, Corrensstrasse 46, D-48149, Münster, Germany
[d] Energy Storage & Distributed Resources Division, Lawrence Berkeley National Laboratory, 1 Cyclotron Road, CA, 94720, Berkeley, USA

ARTICLE INFO

Keywords:
Lithium-metal batteries
Dendrite
X-ray nano-tomography

ABSTRACT

A lithium-metal composite is proposed, which includes a carbon-nitrogen modified stainless steel mesh (CNSSM) favoring homogeneous lithium-metal nucleation and growth of fresh and dense lithium deposits when employed as anode for lithium-metal batteries. This novel approach is able to overcome the usual drawbacks linked to the preexisting passivation layer at the surface of lithium. Instead, a favorable interphase with low resistivity is formed with the electrolyte, and the CNSSM modified lithium-metal composite (CNSSM-Li) results in low-voltage hysteresis (±24 mV) and allows stable and dendrite-free lithium electrodeposition. The performance of lithium-metal batteries demonstrates the outstanding capabilities of the novel CNSSM-Li electrode in promoting cell energy density and cycling stability. In addition, advanced X-ray nano-tomography is employed to characterize the composition and morphology changes of this electrode upon plating.

1. Introduction

Lithium-metal batteries (LMBs) [1] are attracting increasing attention as high energy storage candidates for electric vehicles and smart electrical grids [2,3]. Because of their higher achievable energy densities, LMBs currently appear to be the most probable alternative to lithium-ion batteries [4–6]. Lithium possesses an ultra-high theoretical specific capacity (3860 mAh g^{-1}) with a low standard potential (−3.04 V *vs.* standard hydrogen electrode) [7,8]. However, the operation of lithium-metal anodes is challenging. The lithium-metal easily passivate in dry air during extrusion or foil calendaring, forming a "native" layer mostly made of Li_2O. This layer evolves further upon contact with the electrolyte to form a protective layer—the so-called "Solid Electrolyte Interphase" (SEI)—that can prevent extensive lithium reduction in contact with many aprotic solvents and electrolytes [9–12]. This layer allows Li^+ transport while, in principle, blocking electrons and other electrolyte species. In fact, graphite operates at a potential similar to that of lithium metal, and the formation of an SEI is also involved to stabilize the electrode/electrolyte interface [13]. In this case, the SEI, which forms during the first lithiation from the reaction between the electrolyte and the surface of graphite, can be easily optimized. However, the SEI is continuously evolving in the case of lithium [14], and its properties depend highly on the storage conditions of the lithium foil, the preparation and handling of the lithium electrodes, and the cycling and storing conditions. For example, a lithium foil kept in a dry room exhibited different behavior compared with one kept in a glovebox, owing to different surface chemistry evolutions [15]. In addition, the separator, in physical contact with the electrode, might also affect SEI evolution [16] and result in a high variability of the lithium metal surface even before electrolyte contact. Its high reactivity makes studies on lithium metal especially challenging, because it is difficult to produce a "fresh" and planar lithium surface to fully control the chemistry evolution of the interface with the electrolyte. Some attempts have been made by cutting a lithium ingot [17], and research laboratories often attempt to "reset" the SEI history by either calendaring the lithium foil or scratching its surface prior to cell assembly. Unfortunately, these techniques leave behind SEI residues, and even "pristine" commercial 50-μm foils often exhibit a "marbled" surface as

* Corresponding author.
** Corresponding author.
*** Corresponding author.
E-mail addresses: e.paillard@fz-juelich.de (E. Paillard), r_kostecki@lbl.gov (R. Kostecki), jie.li@fz-juelich.de (J. Li).

https://doi.org/10.1016/j.nanoen.2019.104172
Received 17 May 2019; Received in revised form 2 October 2019; Accepted 4 October 2019
Available online 10 October 2019

the former surface and SEI stretch during calendaring [15] or rolling [18]. Even fresh lithium foil "from the roll" contains fissures and surfaces cracks [19]. As a result, the reproducibility and universality of the findings on the lithium metal surface are questionable.

The SEI on lithium metal, however, is extremely critical, because it impacts the impedance for Li^+ transport (and the corresponding charge transfers) and the homogeneity of electrodeposition (*i.e.*, formation of dendrites and mossy lithium during cycling) [20,21,22]. Fast dendrite (tip) growth occurs when the plating current reaches a limiting current, as a result of the salt concentration gradient [23]. Lithium inhomogeneous deposition [15,24], however, can occur well below this limiting current [25]. It is, in fact, believed that inhomogeneity in the SEI contributes to the initial inhomogeneity of current densities [11,24,26–28] that might lead to protrusion (bottom growth) formation. Protrusions, in turn, result in SEI cracking and thus, locally, to a lower resistance for lithium transport. Lithium might even locally disappear as a result of higher local current densities and trigger dendrite (tip) growth [26], following local concentration gradients (*i.e.*, resulting in mossy lithium as a combination of protrusion and, local depletion). Thus, for preventing fast HSAL growth at high current rates, single ion conductors are used for preventing any lithium depletion at the lithium/electrolyte interface [29–31]. However, preventing protrusion and obtaining fully homogeneous plating depend on the mechanical properties of the electrolyte and of the SEI. For this reason, several approaches must be combined for high-performance LMBs.

In this study, we address the formation of a "fresh" lithium surface obtained by homogeneous electroplating and the formation of an SEI that does not depend on the history of the lithium foil. We developed a modified lithium foil, where plating occurs homogeneously onto a lithiophilic substrate rather than through the SEI evolved from the "native" protective layer of lithium. Thus, the nucleation overvoltage (on a mismatching crystalline structure) that would favor fast HSAL growth [32], as well as plating through a poorly controlled SEI, have been avoided. To realize that outcome, the bulk of the lithium electrode is kept in contact with a conductive carbon-nitrogen modified stainless steel mesh (CNSSM) onto which a coating allows easy lithium nucleation. As a result, a fresh and ionically conductive SEI is formed on top of a homogeneous lithium deposit, allowing stable cycling performance and low impedance.

2. Results and discussion

Fig. 1a gives a schematic representation of the fabrication process of the CNSSM and the final carbon-nitrogen modified stainless steel mesh and lithium composite electrode (CNSSM-Li). The stainless steel mesh (SSM) was first carbonized and covered with a dense functional layer, then pressed onto lithium foil via mechanical pressing. Experimental details are explained in the Supporting Information. Digital camera images of SSM, CNSSM, and CNSSM-Li are shown in Fig. 1b–d, and the corresponding scanning electron microscopy (SEM) images are given in Fig. 1e–g. After carbon-nitrogen coating, the surface of the CNSSM became rougher, and an outer layer can be clearly seen in the cross-sectional SEM image (Fig. 1f inset). The diameter of the CNSSM grew from 35 μm to ~40 μm, and the thickness of the carbon-nitrogen outer layer was ~1 μm. In the bulk, the stainless steel became granular as a tempered sorbite structure, while two microstructures can be differentiated. The grains in the outer zone appear larger owing to the permeation of carbon atoms from the surface, leading to the formation of Fe_3C [33]. Fig. 1g shows a top-view SEM image of the CNSSM-Li electrode. The CNSSM partly penetrated into the foil, and the bare lithium can be seen through the void of the modified mesh.

Fig. 2a shows the first-order Raman spectrum of the CNSSM. Two bands, at ~1345 cm^{-1} and ~1570 cm^{-1}, correspond to the D- and G-bands of carbon. The D-band corresponds to sp3 carbons (as in amorphous carbon), whereas the G-band indicates the presence of sp2 carbon. The intensity ratio between the D- and G-bands (I_D/I_G) is often used to evaluate the disorder degree in the material. The high I_D/I_G ratio (0.37) in this case implies a relatively large ratio of disordering in the CNSSM outer layer, which may originate from the doped nitrogen atoms [34]. In addition, many spectral features corresponding to nitrogen-containing groups are well defined. The shoulder of the D-band (*i.e.,* the D′-band at 1638 cm^{-1}), presented in Fig. 2a inset, appears via an intra-valley double-resonance in the presence of nitrogen-induced defects, such as the pyrrolic-N [35]. Furthermore, the appearance of a defect-related band as a combination of modes (D + D′) at ~2940 cm^{-1} further proves the insertion of nitrogen atoms into the coated layer [36,37]. The presence of amorphous carbon and carbon-nitrogen components (g-C_3N_4 graphitic carbon nitride) is also confirmed by XRD (shown in Fig. S1) by the appearance of characteristic peaks at 26.5° [33] and 27.8° [38], respectively. The diffraction peak of Fe_3C [33] confirms the reaction between carbon and stainless steel via pyrolysis [39].

The chemical composition of the CNSSM surface was probed by X-ray

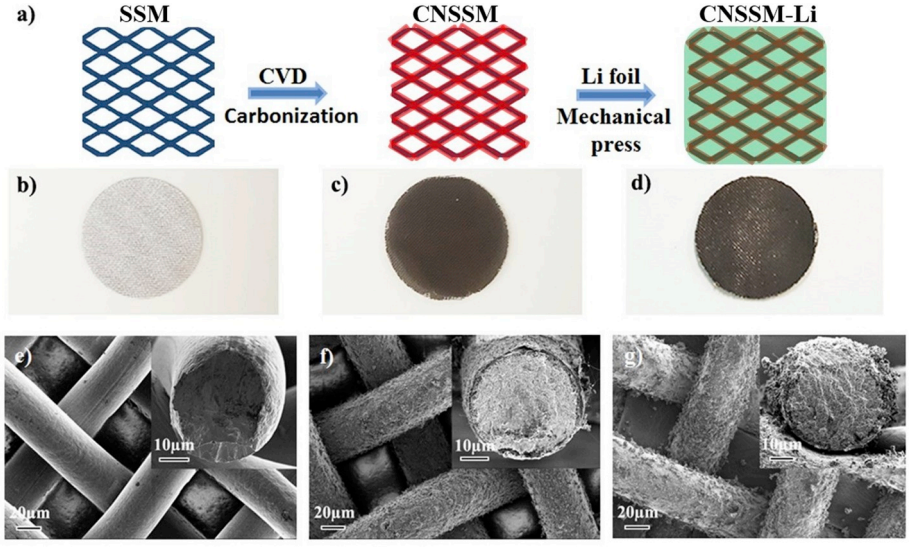

Fig. 1. a) Schematic illustration of the fabrication process of the CNSSM-Li composite electrode. Digital camera images of **b)** SSM, **c)** CNSSM, and **d)** CNSSM-Li composite electrode. SEM image top views and cross-sections (insets) of **e)** SSM, **f)** CNSSM, and **g)** CNSSM-Li composite electrode.

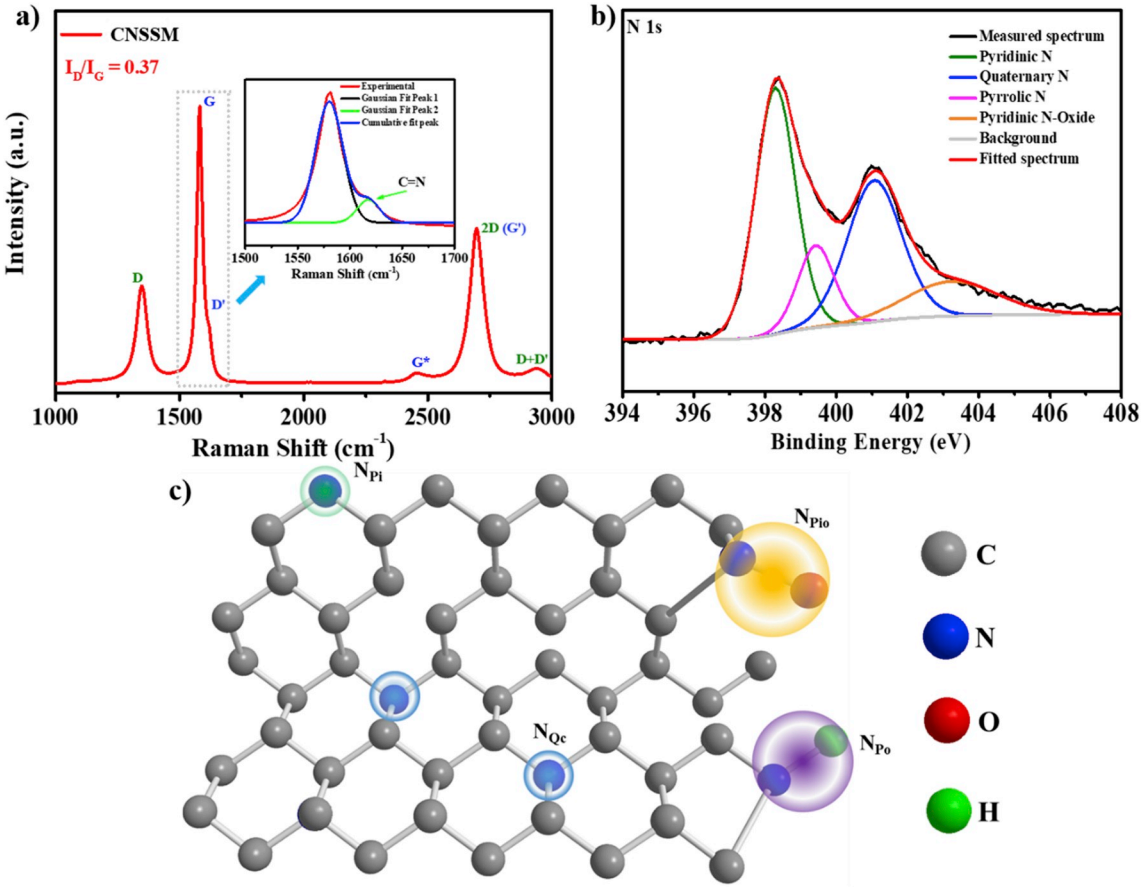

Fig. 2. **a)** Raman spectrum of the CNSSM; the inset shows the fitted curves between 1500 cm^{-1} and -1700 cm^{-1}. **b)** N1s XPS spectrum and the corresponding fitted spectrum. **c)** Schematic representation of a carbon network with different types of nitrogen atoms (N_{Pi}: Pyridinic-N; N_{Po}: Pyrrolic-N; N_{Qc}: Quaternary-N (center); N_{Pio}: Pyridinic-N oxide) doped in.

photoelectron spectroscopy (XPS), and the spectra are shown in Fig. 2b. The N1s spectrum indicates the presence of nitrogen atoms in CNSSM, with four peaks centered at 398.3 eV (pyridinic-N), 399.4 eV (pyrrolic-N), 401.1 eV (quaternary-N center), and 403.8 eV (pyridinic-N oxide) [40]. The CHN analysis data (Table S3) confirm the presence of carbon (17.55 wt%), nitrogen (1.46 wt%), and a small amount of hydrogen (0.22 wt%). Although the nitrogen content is low, pyridinic-N and pyrrolic-N are expected to lower the lithium nucleation energy compared to other carbon-based composites [41]. Based on Raman, XRD, and CHN analyses, a representation of the structure of the N-doped carbon network is proposed in Fig. 2c.

2.1. X-ray nano-tomography

Despite the nano-scale spatial resolution of the SEM images, it is difficult to distinguish between carbon, plated lithium metal, and steel. Moreover, SEM is limited to surfaces and provides little insight into the bulk of the modified lithium composite. Although the focused ion beam (FIB) can be used to obtain cross-sectional images, obtaining information on the bulk structure is invasive (because etched materials tend to redeposit onto the sample). Hence, to probe the bulk of the electrode before and after lithium plating, X-ray holographic nano-tomography was used as a non-invasive characterization technique. Experiments were done at the ID16A-NI line at ESRF (European Synchrotron Radiation Facility, Grenoble, France), at 17 keV with a focus size of about 27 nm (H) x 37 nm (V). The ID16A-NI line is equipped with a pair of multilayer-coated Kirk-Baez mirrors to focus the beam with 1% energy bandwidth, achieving an intensive flux of 2×10^{12} photons s^{-1} [42,43].

Fig. 3 a) and b) compare virtual cross-sections reconstructed from the nano-tomographic measurements (the whole volumes are shown in the supplementary video) for both a pristine CNSSM-Li composite and a CNSSM-Li composite after 2 h of lithium electrodeposition at 1 mA cm^{-2}. For better contrast, the lithium and carbon-nitrogen phases are colored sandy brown and green, respectively. The virtual cross-section of the pristine CNSSM-Li allows the lithium metal and stainless steel domains to be identified through the grayscale differences and edge contrast. The bright areas in the lithium metal correspond to internal cracks, likely due to the manufacturing process of the CNSSM-Li composite. The stainless steel rod exhibits coaxial layers, in agreement with the SEM cross-sections. The external carbon-nitrogen coated layer, of ~1 μm in thickness can be seen, as can the unmodified residual (black) stainless steel at the core of the wire. In between, the dark gray region corresponds to modified stainless steel, where the color deepens gradually, which is consistent with a decrease in carbon content from surface to core. After 2 h of lithium electrodeposition at 1 mA cm^{-2}, the coating layer cannot be distinguished anymore, probably because lithiation of the carbonaceous coating changes its electron density. Most importantly, it can be seen from both the virtual cross-sections of selected images and the 3D tomographic reconstructed result (Fig. 3d) that a significant amount of lithium has been plated (2 mAh cm^{-2} correspond to ~10 μm of lithium), and the mesh is fully embedded into the deposit. It is also remarkable that no dendrite has formed despite the inducement of inhomogeneities by pressing the CNSSM (*e.g.*, cracks in the SEI, partial covering of the lithium metal foil, and pores in the bulk of the lithium metal). Instead, a rather homogenous and dense deposit is observed. The growth of electrodeposited lithium is mainly around the CNSSM without obvious volume expansion due to the formation of thick porous and mossy lithium structure. This suggests that the CNSSM can successfully

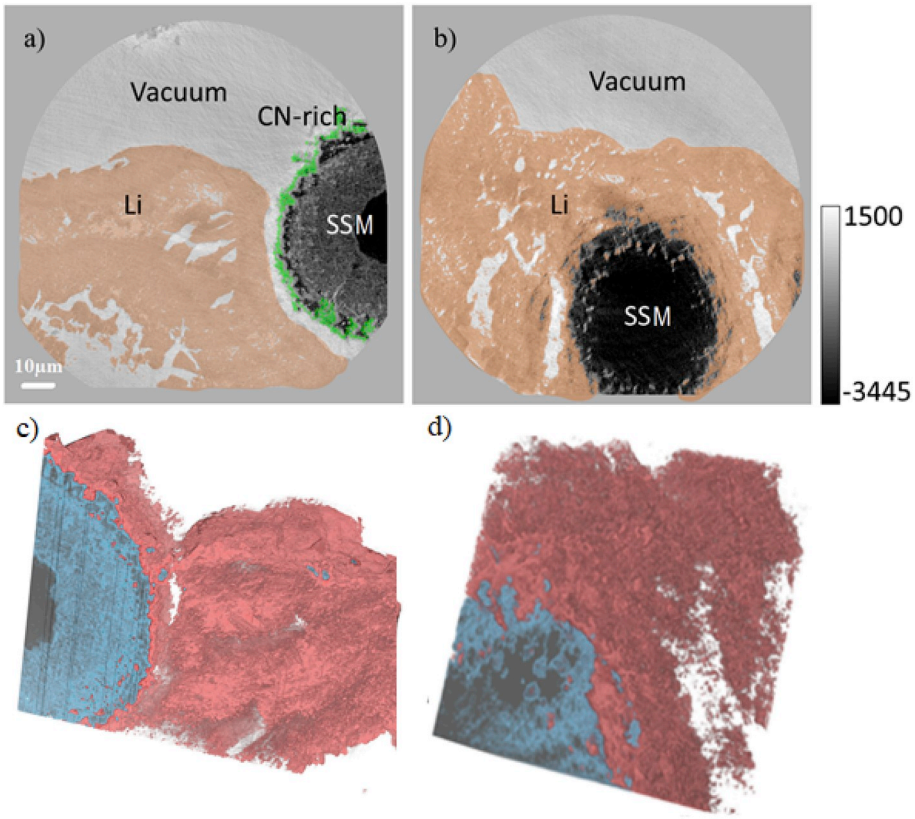

Fig. 3. Virtual cross-sections from X-ray holographic nano-tomography on **a)** a pristine CNSSM-Li composite, and **b)** a CNSSM-Li composite after 2 h of Li electrodeposition at 1 mA cm^{-2}. Li: lithium metal (sandy brown); CN-rich: carbon-nitrogen-rich coating layer (green); CNSSM: carbon-nitrogen modified stainless steel (gray); SSM: stainless steel mesh (black). The scale bar of electro density applies to all panels. Rendering of the 3D tomographic reconstructed results from **c)** pristine CNSSM-Li composite, and **d)** CNSSM-Li composite after 2 h of Li electrodeposition at 1 mA cm^{-2}. Li: lithium metal (coral); CNSSM: carbon-nitrogen modified stainless steel (pale blue); SSM: stainless steel (dim gray).

direct the lithium plating and prohibit the growth of dendritic lithium. Moreover, the clearly identified dim-gray and pale-blue regions (Fig. 3c) spread and diffused after lithium electrodeposition (Fig. 3d), which suggests a lithium storage capability of the Fe_3C [33,44] phase and corrosion behavior of stainless steel in lithium salt electrolyte [45].

2.2. Electrochemical performance of CNSSM-Li composite electrodes

To compare the electrochemical performance of CNSSM-Li to the performance of other lithium-metal electrodes, bare Li-foil (Li), stainless steel mesh (SSM-Li), and carbon nanofibers (CF–Li) with pressed lithium were prepared (see the Supporting Information). The cycling performance of Li, SSM-Li, CF-Li, and CNSSM-Li symmetric cells are provided in Fig. 4a. At a current density of 0.5 mA cm^{-2}, the initial voltage-time profiles of Li and SSM-Li exhibit large lithium electrodissolution/electrodeposition voltage hysteresis, which suggests a high Li^+ transport impedance and will inevitably result in low energy efficiency [46]. After the initial cycles, the hysteresis gradually decreases, because lithium plates in the form of mossy lithium with extended surface area and "fresh" SEI, thus reducing interfacial resistance. After 100 h, however, the hysteresis of SSM-Li starts increasing again as electrolyte is consumed at the extended interface, and degradation products accumulate leading to performance decay. The same behavior is observed with the CF-Li electrode. In contrast, the CNSSM-Li cell reaches 300 h of stable cycling with symmetrical lithium electrodissolution/electrodeposition profiles. Such flat, stable, and symmetrical cycling performance indicates that well-controlled lithium electrodissolution/electrodeposition is achieved with the CNSSM-Li composite electrodes. The voltage hysteresis difference between Li foil and CNSSM-Li is even more obvious at a higher current density (1 mA cm^{-2}), where the Li electrode shows an increasing hysteresis that reaches 15 times that of CNSSM-Li after 200 h of cycling (see Fig. S2 in the Supporting Information). Figs. S3 and S4 show the top-down and cross section SEM images of a CNSSM-Li electrode after 1 h lithium plating at 1 mA cm^{-1}. Lithium filled the CN-rich region and was homogeneously deposited around the CNSSM wire. As a result, the CNSSM-Li composite efficiently stabilizes the cycling of lithium metal and significantly limits the increase of voltage hysteresis. The modification contributes to a lower nucleation overpotential, leading to homogeneous nucleation and thus limited surface area growth with plating, as suggested by the tomography results.

Fig. 4b and c compare the 1st and 100th cycle voltage profiles for the four cells. The CF-Li cell shows a much lower hysteresis in both figures compared with the Li and SSM-Li cells because of the lower local current density due to the larger surface area of the carbon nanofiber [19]. Notably, the CNSSM-Li cell exhibits the lowest hysteresis (about ±24 mV vs. Li/Li^+) and a stable voltage plateau during cycling. Electrochemical impedance spectroscopy (EIS) measurements were carried out on all the cells before cycling and after the 1st cycle (Fig. 4d and e). The overall impedance of the cell with pristine Li electrodes is much higher than that of the SSM-Li, CF-Li, and CNSSM-Li cells. Because of the presence of a native Li_2O and Li_2CO_3 layer on the Li foil surface [47,48], the interfacial resistance of the Li electrode is about 414 Ω cm^2. In comparison, SSM-Li shows low interfacial resistances of only 82 Ω cm^2. For the CF-Li, it provides a large surface area, which reduces the local current density and decreases the areal mass transfer resistance. While the lithiophilic functional group from CNSSM-Li can easily bond to lithium ions via self-reaction and lead to a highly ionic conductive surface. As a result, the interfacial resistance of both CF-Li and the CNSSM-Li composite electrode are only 24 Ω cm^2, and the cells present a smaller hysteresis compared with the others and maintain low resistances after the 1st cycle. Although the overvoltage is significantly reduced by involving carbon nanofibers in the CF-Li electrode, it increases after 100 h of cycling. The highest overvoltage is −75 mV vs. Li/Li^+ (Fig. 4c), which is more than three times higher compared to the cell using the CNSSM-Li composite electrode. Owing to the large surface area provided by the carbon nanofibers, the cumulative SEI layer formation can result in an almost infinite volume change. Consequently, excessive SEI growth

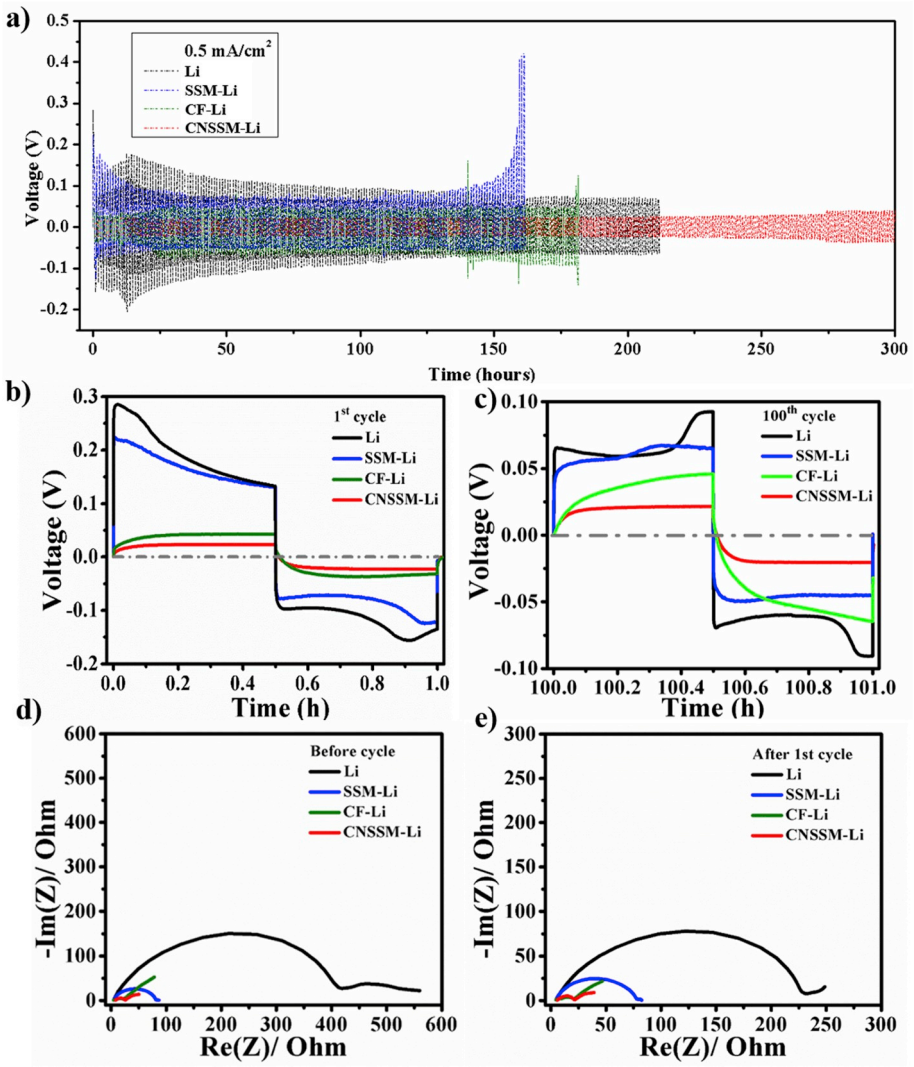

Fig. 4. a) Lithium electrodissolution/electrodeposition cycles for symmetrical Li||Li cells using pristine Li foil electrode, SSM-Li, CF-Li, or CNSSM-Li electrodes at ±0.5 mA cm^{-2}. Corresponding voltage profiles of **b)** the 1st and **c)** the 100th cycles. **d)** Nyquist plots of the symmetrical cells before cycling and e) after the 1st cycle. Frequency range: 10 kHz–100 mHz.

leads to drastically increased voltage hysteresis associated with strong electrolyte consumption.

2.3. Performance of LMB cells using the CNSSM-Li electrode

The type of cathode material affects the performance of LMB cells [49]. Because symmetrical cell data are not sufficient, cells using Li or CNSSM-Li as anode material and $LiFePO_4$ (LFP) as cathode material were assembled and cycled between 2.5 V and 4.1 V (Fig. 5a). Compared to the LFP||Li cell, the LFP||CNSSM-Li cell exhibits a significantly improved rate capability with much reduced voltage hysteresis. The two cells behave similarly in terms of specific capacity at a low current rate of 1 C (1 C = 170 mA g^{-1}), but, at 10 C, the LFP||CNSSM-Li cell achieves a discharge capacity of 76 mAh g^{-1}, while the LFP||Li cell only delivers 67 mAh g^{-1}. The inset in Fig. 5a compares the hysteresis in selected voltage ranges at rates of 1 C and 10 C for the two cells. Similar hysteresis values of 187 mV and 132 mV were obtained from LFP||Li and LFP||CNSSM-Li cells at 1 C, but a larger difference (773 mV for the bare Li electrode and 347 mV for the CNSSM-Li electrode) is observed at 10 C. With increased discharge capacity and voltage, the output energy of LFP||CNSSM-Li cells is significantly increased at high current density. The improvement is also confirmed by the much flatter voltage plateau of the cells assembled with CNSSM-Li (Fig. 5b). A "bump" appears in the curve of the LFP||Li cell in the initial charging process, independent on the current applied. Improved stability can be achieved by using CNSSM-Li composite electrodes; no comparable "bump" is observed in any of the curves under different currents. Full charge-discharge profiles are shown in Fig. S5 in the Supporting Information.

Battery cells with other cathodes—$LiMn_2O_4$ (LMO; Fig. S6 in the Supporting Information) and $LiNi_{0.66}Co_{0.2}Mn_{0.2}O_2$ (NCM622; Fig. S8)—were also assembled and evaluated in this work. The Coulombic efficiencies and average discharge voltages are shown in Fig. 5c. No obvious differences in Coulombic efficiency for the cells prepared with Li vs. CNSSM-Li can be identified. However, a drop in average discharge voltage is apparent. At 2500 mA g^{-1}, the LMO||Li and NCM622||Li cells exhibit initial average discharge voltages of 3.82 V and 3.6 V, and enhancements can be seen in cells with the CNSSM-Li electrode: to 3.93 V for the LMO||CNSSM-Li cell and to 3.77 V for the NCM622||CNSSM-Li cell. In addition, CNSSM-Li provides higher discharge capacity in cells with both LMO and NCM622 (see Figs. S6 and S8 in the Supporting Information). Because the enhancements of both capacity retention and average discharge voltage are independent of the cathode materials, the improvement is explicitly governed by the CNSSM-Li composite electrodes. Fig. 5d compares the long-term cycling stability of the LFP||Li and LFP||CNSSM-Li cells. The cell with the CNSSM-Li composite electrode presents a slightly higher initial capacity at 10 C (89 mAh g^{-1}) but

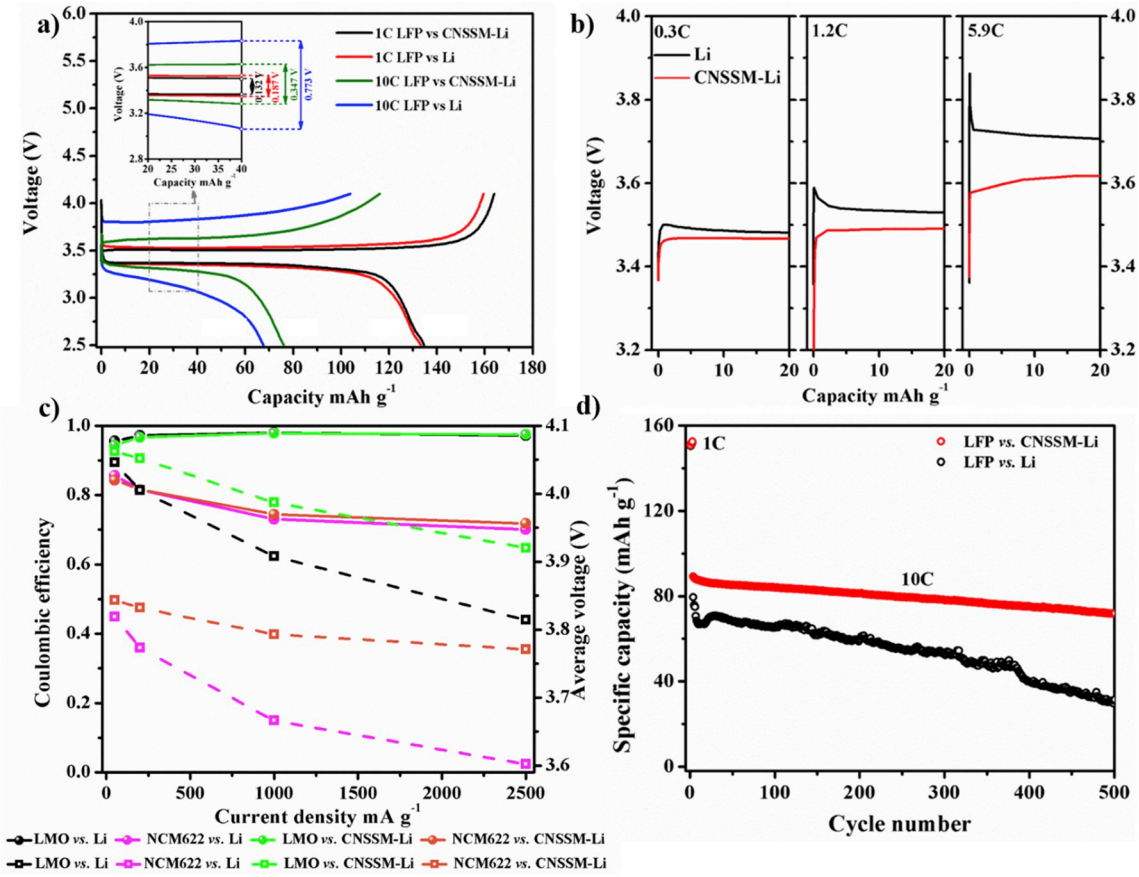

Fig. 5. a) Voltage profile comparison of the LFP||Li cells and LFP||CNSSM-Li cells at 1 C (1C = 167 mA g^{-1}) (nominal current = 0.334 mA cm^{-2}) and 10 C; the hysteresis in the voltage profile is enlarged and shown in the inset. **b)** Comparison of the enlarged voltage profiles for LFP||Li cells and LFP||CNSSM-Li cells at 0.3 C (50 mA g^{-1}), 1.2 C (200 mA g^{-1}), and 5.9 C (1000 mA g^{-1}) in the initial charge. Detailed potential profiles are shown in Fig. S5 in the Supporting Information. **c)** Coulombic efficiency (solid spheres) and average discharge voltages (hollow squares) of four different full cells at current densities of 50 mA g^{-1}, 200 mA g^{-1}, 1000 mA g^{-1}, and 2500 mA g^{-1}, *i.e.*, spinel LMO||Li (black) (1C = 148 mA g^{-1}, nominal current = 0.296 mA cm^{-2}), layered NCM622||Li (pink) (1C = 180 mA g^{-1}, nominal current = 0.36 mA cm^{-2}), spinel LMO||CNSSM-Li (light green), and layered NCM622||CNSSM-Li (orange). **d)** Cell cycling performance of LFP paired with Li and CNSSM-Li composite electrode. The mass loadings of LFP, LMO and NCM622 cathode are *ca.* 2 mg cm^{-2}.

a much longer cycle life, with a capacity retention of 80.9% after 500 cycles. The cell with the bare Li electrode shows a rapid decline after 170 cycles and dies soon thereafter. Thus, the cell with the CNSSM-Li composite shows better rate capability, more stable cycling performance, and a higher average discharge voltage, demonstrating its great potential for overcoming the LMB dilemma.

3. Conclusion

The use of a CNSSM matrix results in uniform lithium electrodeposition and guides homogeneous lithium growth. Synchrotron X-ray nano-tomography provides clear insight into the evolution of the morphology and components of the CNSSM-Li composite after lithium electrodeposition. With this technique, the inner structure of the prepared CNSSM-Li composite and lithium electrodeposited electrode can be directly visualized in three dimensions. The carbon-nitrogen functional groups, such as pyridinic nitrogen and pyrrolic nitrogen, have been shown to adsorb a considerable amount of Li^+ ions, which regulates the nucleation of metallic lithium. The network structure provided by modified SSM can further lower local current density, reduce the charge transfer resistance, and accommodate the volume expansion upon lithium plating. A low-voltage hysteresis can be obtained when using CNSSM-Li as the anode in both symmetrical cells and full cells constructed with conventional cathode materials, especially at increased current density. Furthermore, improved output energy and stable cycling performance over 500 cycles demonstrate the remarkable role of CNSSM-Li for LMBs. The improvements presented here are not only a guide for designing modified electrode structures for LMBs, but also for designing other metal-containing energy-storage systems.

Declaration of competing interest

The authors declare that they have no known competing financial interests or personal relationships that could have appeared to influence the work reported in this paper.

Acknowledgement

X.H. and R.K. were supported by the Assistant Secretary for Energy Efficiency and Renewable Energy, Vehicle Technologies Office, under the Advanced Battery Materials Research (BMR) Program, of the U.S. Department of Energy under Contract No. DE-AC02-05CH11231f.

Appendix A. Supplementary data

Supplementary data to this article can be found online at https://doi.org/10.1016/j.nanoen.2019.104172.

References

[1] B. Liu, J.-G. Zhang, W. Xu, Joule 2 (2018) 833.
[2] M. Winter, B. Barnett, K. Xu, Chem. Rev. 118 (23) (2018) 11433.

[3] R. Schmuch, R. Wagner, G. Hörpel, T. Placke, M. Winter, Nat. Energy 3 (2018).
[4] J. Betz, G. Bieker, P. Meister, T. Placke, M. Winter, R. Schmuch, Adv. Energy Mater. 1803170 (2019) 1.
[5] R. Wagner, N. Preschitschek, S. Passerini, J. Leker, M. Winter, J. Appl. Electrochem. 43 (2013) 481.
[6] T. Placke, R. Kloepsch, S. Dühnen, M. Winter, J. Solid State Electrochem. 21 (2017) 1939.
[7] J.M. Tarascon, M. Armand, Nature 414 (2001) 359.
[8] W. Xu, J. Wang, F. Ding, X. Chen, E. Nasybulin, Y. Zhang, J.G. Zhang, Energy Environ. Sci. 7 (2014) 513.
[9] E. Peled, J. Electrochem. Soc. 126 (1979) 2047.
[10] E. Peled, S. Menkin, J. Electrochem. Soc. 164 (2017). A1703.
[11] B. M. Winter, 2009, 223, 1395.
[12] H. Liu, X. Wang, H. Zhou, H. Lim, X. Xing, Q. Yan, Y.S. Meng, P. Liu, ACS Appl. Energy Mater. 1 (2018) 1864.
[13] J.R. Fong, R. von Sacken, U. Dahn, J. Electrochem. Soc. 137 (1990) 2009.
[14] K.-C. Möller, T. Hodal, W.K. Appel, M. Winter, J.O. Besenhard, J. Power Sources 97–98 (2001) 595.
[15] L. Grande, J. Von Zamory, S.L. Koch, J. Kalhoff, E. Paillard, S. Passerini, ACS Appl. Mater. Interfaces 7 (2015) 5950.
[16] M. Kirchhöfer, J. Von Zamory, E. Paillard, S. Passerini, Int. J. Mol. Sci. 15 (2014).
[17] M.S. Ding, S.L. Koch, S. Passerini, Electrochim. Acta 240 (2017) 408.
[18] J. Becking, A. Gröbmeyer, M. Kolek, U. Rodehorst, S. Schulze, M. Winter, P. Bieker, M.C. Stan, Adv. Mater. Interfaces 4 (2017) 1700166.
[19] M.H. Ryou, Y.M. Lee, Y. Lee, M. Winter, P. Bieker, Adv. Funct. Mater. 25 (2015) 834.
[20] H. Liu, X. Yue, X. Xing, Q. Yan, J. Huang, V. Petrova, Energy Storage Mater. 16 (2019) 505.
[21] H. Liu, H. Zhou, B. Lee, X. Xing, M. Gonzalez, P. Liu, ACS Appl. Mater. Interfaces 9 (2017) 30635.
[22] G. Bieker, M. Winter, P. Bieker, Phys. Chem. Chem. Phys. 17 (2015) 8670.
[23] J.-N. Chazalviel, Phys. Rev. A 42 (1990) 7355.
[24] P. Bai, J. Li, F.R. Brushett, M.Z. Bazant, Energy Environ. Sci. 9 (2016) 3221.
[25] P. Barai, K. Higa, V. Srinivasan, Phys. Chem. Chem. Phys. 19 (2017) 20493.
[26] M. Rosso, T. Gobron, C. Brissot, J.N. Chazalviel, S. Lascaud, J. Power Sources 97–98 (2001) 804.
[27] M.D. Tikekar, S. Choudhury, Z. Tu, L.A. Archer, Nat. Energy 1 (2016) 16114.
[28] J. Heine, S. Krüger, C. Hartnig, U. Wietelmann, M. Winter, P. Bieker, Adv. Energy Mater. 4 (2014) 1.
[29] H.D. Nguyen, G.T. Kim, J. Shi, E. Paillard, P. Judeinstein, S. Lyonnard, D. Bresser, C. Iojoiu, Energy Environ. Sci. 11 (2018) 3298.
[30] D. Benrabah, S. Sylla, F. Alloin, J.-Y. Sanchez, M. Armand, Electrochim. Acta 40 (1995) 2259.
[31] R. Bouchet, S. Maria, R. Meziane, A. Aboulaich, L. Lienafa, J.P. Bonnet, T.N. T. Phan, D. Bertin, D. Gigmes, D. Devaux, R. Denoyel, M. Armand, Nat. Mater. 12 (2013) 452.
[32] L. Grande, E. Paillard, G.T. Kim, S. Monaco, S. Passerini, Int. J. Mol. Sci. 15 (2014) 8122.
[33] X. Zhao, D. Xia, J. Yue, S. Liu, Electrochim. Acta 116 (2014) 292.
[34] A.V. Okotrub, L.G. Bulusheva, I.A. Kinloch, I.P. Asanov, A.G. Kurenya, A. G. Kudashov, X. Chen, H. Song, Phys. Stat. Sol. (B) 245 (10) (2008) 1971–1974, https://doi.org/10.1002/pssb.200879592.
[35] B.J. Matsoso, K. Ranganathan, B.K. Mutuma, T. Lerotholi, G. Jones, N.J. Coville, RSC Adv. 6 (2016) 106914.
[36] E.O. Hall, N.J. Petch, K.W. Jacobsen, S. Yip, M.A. Meyers, A. Mishra, D.J. Benson, P.G. Sanders, J.A. Eastman, J.R. Weertman, C.C. Koch, K.M. Youssef, R. O. Scattergood, K.L. Murty, Y.F. Shen, L. Lu, Q.H. Lu, Z.H. Jin, K. Lu, L. Lu, Y. Shen, X. Chen, L. Qian, K. Lu, J. Chen, L. Lu, K. Lu, A. Misra, X. Zhang, D. Hammon, R. G. Hoagland, M.A. Meyers, K.K. Chawla, M. Horton, U. Saddle, L. Lu, K. Lu, N. Hansen, N. Tsuji, R.K. Mishra, S.A.S. Asif, O.L. Warren, A.M. Minor, J. Mizera, J. W. Wyrzykowski, N.R. Tao, K. Lu, P.M. Hazzledine, L. Lu, Y. Shen, S. Suresh, J. Li, A. Samanta, H.G. Kim, S. Suresh, Z. Jin, W. Pantleon, B. Ralph, X. Si, Science 323 (2009) 610.
[37] I. Bobrinetskiy, A.V. Emelianov, N. Otero, P.M. Romero, Appl. Phys. Lett. 107 (2015).
[38] L. Ge, C. Han, J. Liu, Y. Li, Appl. Catal. A Gen. 409–410 (2011) 215.
[39] L. Maya, D.R. Cole, E.W. Hagaman, J. Am. Ceram. Soc. 74 (1991) 1686.
[40] T. Sharifi, G. Hu, X. Jia, T. Wågberg, ACS Nano 6 (2012) 8904.
[41] R. Zhang, X.R. Chen, X. Chen, X.B. Cheng, X.Q. Zhang, C. Yan, Q. Zhang, Angew. Chem. Int. Ed. 56 (2017) 7764.
[42] C. Morawe, R. Barrett, P. Cloetens, B. Lantelme, J.-C. Peffen, A. Vivo, Proc. SPIE (2015) 958803.
[43] P. Cloetens, W. Ludwig, J. Baruchel, D. Van Dyck, J. Van Landuyt, J.P. Guigay, M. Schlenker, Appl. Phys. Lett. 75 (1999) 2912.
[44] A. Kitajou, S. Kudo, J. Hayashi, S. Okada, Electrochemistry 85 (2017) 630.
[45] A.I. Muñoz, J.G. Antón, J.L. Guiñón, V.P. Herranz, Corrosion 59 (2003) 606.
[46] P. Meister, H. Jia, J. Li, R. Kloepsch, M. Winter, T. Placke, Chem. Mater. 28 (2016) 7203.
[47] S. Shiraishi, K. Kanamura, Z.-I. Takehara, J. Appl. Electrochem. 29 (1999) 869.
[48] Y. Li, B. Xu, H. Xu, H. Duan, X. Lü, S. Xin, W. Zhou, L. Xue, G. Fu, A. Manthiram, J. B. Goodenough, Angew. Chem. Int. Ed. 56 (2017) 753.
[49] J. Betz, J. Brinkmann, R. Nölle, C. Lürenbaum, M. Kolek, M.C. Stan, M. Winter, T. Placke, Adv. Energy Mater. (2019) 1900574.